crystal form; L. Huang, E. Kinnucan, N. P. Pavletich, data not shown) and in the E6AP-UbcH7 complex. However, the E6AP hect domain is a monomer in solution, and mutation of a residue (Phe^{727}) making key trimer contacts has little effect on the ubiquitin-thioester bond formation (L. Huang, E. Kinnucan, G. Wang, S. Beaudenon, J. M. Huibregtse, N. P. Pavletich, data not shown). The interactions associated with the formation of the trimer could, in principle, have favored the crystallization of the E6AP-UbcH7 complex in the same E6AP conformation as in the E6AP-alone crystals.

26. Equivalent amounts of purified wild-type and mutant GST-hect proteins were used in an in vitro ubiquitin-thioester assay (*14*). The reactions contained purified baculovirus-expressed human E1 protein, purified UbcH7, ^{32}P-labeled ubiquitin, and ATP. Reactions were incubated at room temperature for 5 to 10 min and stopped with SDS–polyacrylamide gel electrophoresis (PAGE) loading buffer lacking reducing agent. Products were analyzed by SDS-PAGE and autoradiography and quantified with a Molecular Dynamics Phosphoimager. The amounts of ubiquitin-thioester bond formation for the mutants, relative to the wild-type protein, are 0% for C820S, 4% for H818A, 26% for T819A, 31% for F821A, 28% for N822A, 8% for R506A, 7% for E539A, 6% for E550A, and 10% for D607A. Each reaction was repeated three times, with typical error bars of up to 4% of the wild-type activity.
27. J. M. Huibregtse, M. Scheffner, S. Beaudenon, P. M. Howley, *Proc. Natl. Acad. Sci. U.S.A.* **92**, 2563 (1995).
28. J. Clayton-Smith and S. Ramsden, personal communication.
29. P. Fang *et al.*, *Hum. Mol. Genet.* **8**, 129 (1999).
30. P. Malzac *et al.*, *Am. J. Hum. Genet.* **62**, 1353 (1998).
31. J. Wagstaff, personal communication.
32. Z. Nawaz *et al.*, *Mol. Cell. Biol.* **19**, 1182 (1999).
33. On the UbcH7 L1 loop, the Phe^{63} side chain makes van der Waals contacts with the E6AP Leu^{635}, Leu^{639}, Leu^{642}, Phe^{690}, Tyr^{694}, and Ile^{655}; the charged residues of L1, Glu^{60} and Lys^{64}, form hydrogen bonds with each other and with Gln^{661} and Thr^{662} of E6AP in the solvent-exposed end of the E6AP groove.
34. On the UbcH7 L2 loop, Pro^{97} makes van der Waals contacts with Met^{653}, Asp^{641}, and Ser^{638} of E6AP; Ala^{98} makes van der Waals contacts with Met^{653} and Tyr^{645} of E6AP; Lys^{96} forms hydrogen bonds with Asp^{641}; and Lys^{100} forms hydrogen bonds with the backbone carbonyl of Asp^{652}. The H1 helix of UbcH7 contributes minor contacts; its Arg^{6} and Lys^{9} side chains, which have high temperature factors, are within hydrogen-bonding distance of the backbone carbonyl groups of Met^{653} and Asp^{651} of E6AP, respectively. The UbcH7 Leu^{33}, which occurs in a loop (residues 28 to 33) adjacent to the H1 helix, makes a van der Waals contact to the E6AP Pro^{668}.
35. S. C. Johnston, S. M. Riddle, R. E. Cohen, C. P. Hill, *EMBO J.* **18**, 3877 (1999).
36. R. Beal, Q. Deveraux, G. Xia, M. Rechsteiner, C. Pickart, *Proc. Natl. Acad. Sci. U.S.A.* **93**, 861 (1996).
37. Y. Yamamoto, J. M. Huibregtse, P. M. Howley, *Genomics* **41**, 263 (1997).
38. Z. Otwinowski and W. Minor, *Methods Enzymol.* **276**, 307 (1997).
39. CCP4, *Acta Crystallogr.* **D50**, 760 (1994).
40. T. A. Jones, J.-Y. Zou, S. W. Cowan, M. Kjeldgaard, *Acta Crystallogr.* **A47**, 110 (1991).
41. A. T. Brünger *et al.*, *Acta Crystallogr.* **D54**, 905 (1998).
42. P. J. Kraulis, *J. Appl. Crystallogr.* **24**, 946 (1991); D. Bacon and W. F. Anderson, *J. Mol. Graphics* **6**, 219 (1988).
43. A. Nicholls, K. A. Sharp, B. Honig, *Proteins Struct. Funct. Genet.* **11**, 281 (1991).
44. Supported by NIH, the Howard Hughes Medical Institute, the Dewitt Wallace Foundation, the Samuel and May Rudin Foundation, and a Norman and Rosita Winston Foundation fellowship (L.H.). We thank J. Wagstaff at Boston Children's Hospital and S. Ramsden and J. Clayton-Smith at St. Mary's Hospital for the AS mutation data before publication; M. Scheffener for the UbcH7 plasmid; H. Erdjument-Bromage of the Sloan-Kettering Microchemistry Facility for NH_2-terminal sequence analysis; C. Ogata of the National Synchrotron Light Source (NSLS) X4A beamline, M. Sullivan of the NSLS X9B beamline, and T. Earnest, G. McDermott, K. Henderson, and L. Hung at the Advanced Light Source Beamline 5.0.2 for help with data collection; P. Jeffrey for help with synchrotron data collection; and C. Murray for administrative assistance. Coordinates have been deposited with the Protein Data Bank (accession codes 1D5F for E6AP and 1C4Z for the E6AP-UbcH7 complex).

15 September 1999; accepted 12 October 1999

REPORTS

Evidence for a Ubiquitous Seismic Discontinuity at the Base of the Mantle

Igor Sidorin, Michael Gurnis,* Don V. Helmberger

A sharp discontinuity at the base of Earth's mantle has been suggested from seismic waveform studies; the observed travel time and amplitude variations have been interpreted as changes in the depth of a spatially intermittent discontinuity. Most of the observed variations in travel times and the spatial intermittance of the seismic triplication can be reproduced by a ubiquitous first-order discontinuity superimposed on global seismic velocity structure derived from tomography. The observations can be modeled by a solid-solid phase transition that has a 200-kilometer elevation above the core-mantle boundary under adiabatic temperatures and a Clapeyron slope of about 6 megapascal per kelvin.

Seismic studies provide information about the composition, state, and dynamics of Earth's mantle. Global seismic velocity images represent snapshots of mantle convection (*1*), whereas more detailed waveform studies provide evidence for phase transitions, chemical heterogeneity, and partial melting in the mantle (*2–4*). Unfortunately, the interpretation of the structural features of the mantle inferred from seismology is plagued by trade-offs and ambiguities. Most global tomographic inversions do not incorporate seismic discontinuities in the mantle, attributing any associated travel time anomalies to volumetric heterogeneity. Similarly, most waveform modeling uses globally averaged one-dimensional (1D) seismic velocity reference models focusing on isolated regions without consideration of the geographical variations in velocity. This difference between seismic inversion techniques makes it difficult to distinguish localized structure from broader anomalies distributed along the ray paths. As a result, there is poor understanding of the relation between large-scale mantle convection imaged by seismic tomography and the smaller scale processes, which may include chemical heterogeneity, solid-solid phase transitions, and partial melting. The smaller scale processes produce specific signatures in the fine-scale seismic velocity field that is usually explored by waveform modeling.

One such mantle feature is a travel time triplication attributed to a sharp (*5*), 2 to 3% velocity discontinuity about 250 km above the core-mantle boundary (CMB) (*6*). The primary evidence for the triplication is an additional phase, *Scd*, arriving between the direct, *S*, and core-reflected, *ScS*, shear wave phases in about 65° to 83° distance range (*2, 7–9*). The relative timing and amplitudes of the three phases experience significant regional variations. This intermittent triplication may be due to a laterally varying D″ discontinuity (*10*). Alternatively, the observed spatial intermittance of the triplication may be attributed to variations of the local velocity gradients accompanying a small (≈1%) velocity jump (*11*).

The triplication is strong or detectable beneath the circum-Pacific region, which has been associated with zones of faster-than-average velocities at the base of the mantle (Fig. 1), and it is weak or undetectable in anomalously slow regions (*12*). This suggests that the local structure can modulate the strength of the triplication produced by a possibly ubiquitous discontinuity. This poses the question if it is possible to predict the observed geographic patterns in the strength and timing of the phases associated with the triplication by using the structure inferred by tomographic inversions.

We used Grand's shear wave velocity

Seismological Laboratory 252-21, California Institute of Technology, Pasadena, CA 91125, USA.

*To whom correspondence should be addressed. E-mail: gurnis@caltech.edu

model (*13*) to represent the global large-scale seismic velocity structure. Tomographic inversions do not incorporate the *Scd* phase, so that any travel time anomaly arising from a D″ discontinuity is attributed to a volumetric anomaly at the base of the mantle. Given this nonuniqueness of the inferred seismic structure, we "refined" tomography models by adding a discontinuity at a certain level and compensated for its influence on travel times by adjusting the local volumetric anomaly. A physical model predicting the depth of the discontinuity at any given location is needed. A combination of dynamic and seismic modeling suggests that a phase change is a more likely cause for the D″ discontinuity than thermal gradients or a chemically distinct layer at the base of the mantle (*11, 14*). Assuming the D″ discontinuity is caused by a solid-solid phase transition, we used thermal anomalies inferred from tomography models (*15*) to predict its depth variations (*16*). The velocity anomalies provided by the tomography model are mapped onto a fine mesh to ensure that the topography of the incorporated discontinuity is adequately resolved and that each vertical column of the new mesh is perturbed by adding a discontinuity and an appropriate compensation (Fig. 2) (*17*).

To explore how well the described composite model incorporating a first-order discontinuity superimposed on the tomography reproduces seismic observations, we computed 2D synthetic waveforms (*18*) for a variety of ray paths sampling D″ in five different regions (Fig. 1). Differential travel times, $T_{Scd\text{-}S}$ and $T_{ScS\text{-}Scd}$, are obtained from the synthetic waveforms and compared with the corresponding observations. These differentials provide important constraints on the D″ structure, characterizing the heterogeneity and possible topography of the discontinuity at the base of the mantle. We restricted the analysis of the quality of our model predictions to the $T_{Scd\text{-}S}$ differential travel times (*19*) and used the root-mean-square (rms) misfit (*20*) to compare various models in search of a range of the phase transition characteristics most compatible with seismic observations (*21*). We initially focused on the observations for Alaska and Eurasia, because extensive data sets are available for these regions (*22*). These data sets are used to calibrate our model, and the most consistent model is then used to predict travel times in other regions with observations of the D″ triplication. Comparisons of data for Alaska and Eurasia with predictions of models incorporating phase transitions with various characteristics allowed us to select a range of models providing travel time predictions most consistent with observations (Fig. 3). The best predictions are provided by a model incorporating a phase transition with $\gamma_{ph} \approx 6$ MPa/K and $h_{ph} \approx 200$ km. Accordingly, we will refer to the model characterized by these parameters as the "preferred model." However, the variation of the residuals among the models within the shaded region in Fig. 3 is insignificant, and we cannot discriminate between different models with just one average travel time residual. However, these models can be distinguished by looking at the distance dependence of the predicted and observed travel times. We explore the quality of the fit to the observed $T_{Scd\text{-}S}$ differentials predicted by the preferred model and two other models with the smallest travel time residuals (Fig. 3). A two-step approach was used, where we first obtained a least-squares fit to the predicted differential travel times (Fig. 4A) and then compared the fitted curves to the observed travel times. Using this method,

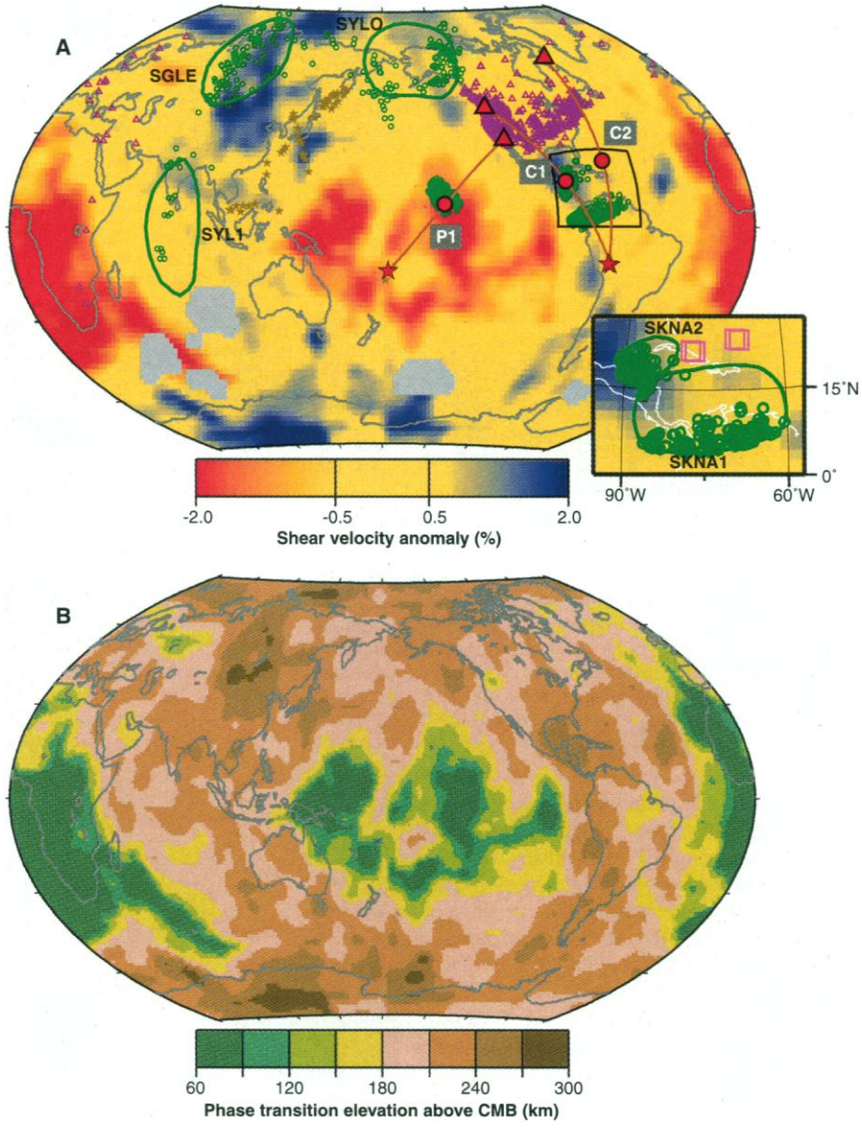

Fig. 1. (**A**) Seismic observations of the D″ triplication: events (stars) and stations (triangles) used in the study. Circles show surface projections of *ScS* bounce points for the paths that are considered (*21*). The regions with strongly observed D″ triplication are shown by green contours and the names of the corresponding seismic 1D reference models (*34*) are given next to the contours. The pink squares in the inset indicate *ScS* bounce points beneath Central America for ray paths that do not show any evidence for a D″ triplication (*8*). The three highlighted paths are used in Figs. 2 and 5B to illustrate the sampled structure at the base of the mantle and its influence on the predicted seismic waveforms. The background color represents the shear velocity in the lowermost 240 km of the mantle (*13*). (**B**) Map of the elevation of the D″ discontinuity above the CMB predicted by the preferred model. The elevations beneath Alaska and Eurasia are lower than suggested by the respective 1D seismic reference models SYLO (243 km) and SGLE (290 km). The elevation of the discontinuity beneath Africa and the central Pacific Ocean is likely underestimated, because the large slow velocity anomaly there (~4%) implies either chemical heterogeneity or partial melt, and our linear scaling between seismic velocity and temperature (*15*) may not be valid.

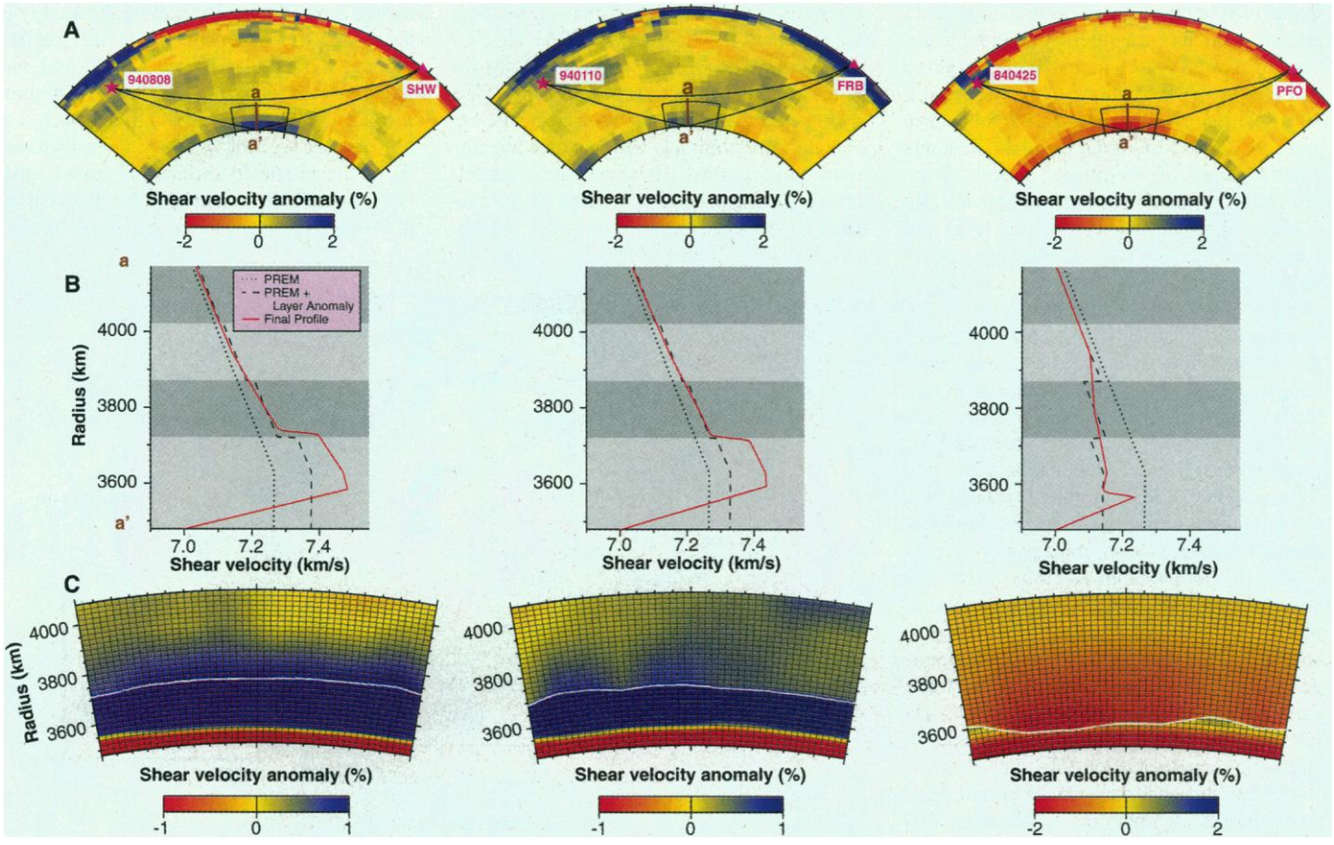

Fig. 2. Shear velocity cross sections along the ray paths highlighted in Fig. 1. (Left) Event 940808 (*8*) to station SHW (path C1); (middle) event 940110 (*8*) to station FRB (path C2); (right) event 840425 (*33*) to station PFO (path P1). (**A**) Cross sections through Grand's tomography model (*13*). Direct (*S*) and core-reflected (*ScS*) rays are shown. (**B**) Perturbing a vertical column to incorporate a discontinuity using cross section a–a′ indicated in (A) as an example. The gray shading shows the layers of the tomography model (*13*). Dotted line shows PREM (*29*); dashed line shows the block anomalies (PREM values with added tomography velocity perturbations); the red solid line shows the final profile obtained by adding a discontinuity and a compensating negative gradient at the base of the mantle (*17*). (**C**) Final composite model (perturbations with respect to PREM) for the region marked in (A). The grid lines of the fine mesh are shown (every other line is plotted horizontally, and one in every 10 is plotted vertically) and the phase boundary is indicated by the white line. The phase transition in (B) and (C) is characterized by h_{ph} = 200 km and γ_{ph} = 6 MPa/K.

we demonstrate that the preferred model provides a significantly better fit to the Eurasian and Alaskan data (Fig. 4B) than a model with a phase boundary at a constant depth (Fig. 4C) or a phase boundary corresponding to a negative Clapeyron slope (Fig. 4D). The other two models have small travel time residuals (Fig. 3) but predict differential travel times that are inconsistent with the data for Eurasia and Alaska. Moreover, the preferred model provides a satisfactory fit to the travel times observed for paths beneath India and the Indian Ocean (Fig. 4E). The predictions of our preferred model are in better agreement with the Indian data than are the travel times corresponding to the 1D seismic reference model originally used to explain the data (*7*).

The structure beneath Central America is peculiar in that the observed travel time patterns vary substantially over relatively short distances. According to Kendall and Nangini (*8*), the travel times for the southern Caribbean can be approximated by a 1D reference velocity model with a 2.75% velocity jump 250 km above the CMB, whereas the travel times for the northern Caribbean can be approximated by a model with a 2.45% velocity jump 290 km above the CMB (Fig. 1, inset). Our preferred model reproduces the observed regional variations in differential travel times in the Caribbean on par with the respective 1D reference models (Fig. 4F) that were constrained by the waveform analysis in addition to travel time picks (*8*).

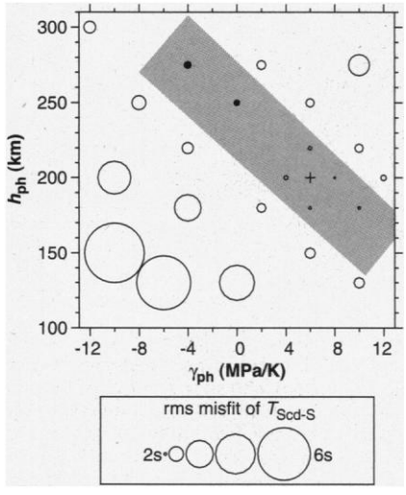

Fig. 3. T_{Scd-S} differential travel time residuals between data for Alaska and Eurasia, and predictions of models with various phase change characteristics (*20*). The shaded region marks the range of models providing the best fit to the data. Models within this region have approximately the same average elevation of the phase boundary above the CMB. They predict T_{Scd-S} with an average residual in the range of 1.8 to 3.4 s. The preferred model with the smallest residual is indicated by a cross. The models marked with solid circles are explored further (Fig. 4).

We used our preferred composite model to

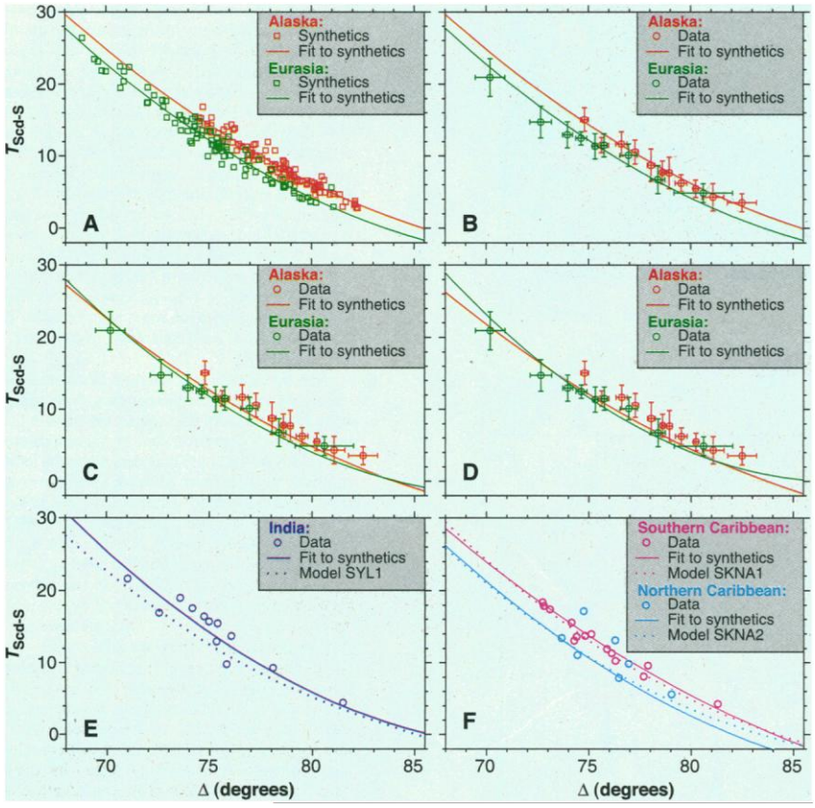

Fig. 4. Comparison of model predictions with observed T_{Scd-S} differential travel times for the source-receiver pairs shown in Fig. 1. **(A)** Polynomial least-squares fit (solid lines) to predictions of the preferred model (h_{ph} = 200 km, γ_{ph} = 6 MPa/K) for Alaska (red) and Eurasia (green). **(B)** Comparison of observed T_{Scd-S} (a running mean is computed in groups of 10; the error bars indicate the standard error) for Alaska and Eurasia with the least squares fit to T_{Scd-S} predicted by the preferred model in (A). **(C)** Same as in (B), except T_{Scd-S} times predicted by model with a phase characterized by h_{ph} = 250 km and γ_{ph} = 0 MPa/K are used. **(D)** Same as in (B), except T_{Scd-S} times predicted by model with a phase characterized by h_{ph} = 275 km and γ_{ph} = −4 MPa/K are used. **(E)** Comparison of observed T_{Scd-S} for India with predictions of the preferred model (solid line) and seismic 1D reference model SYL1 (*34*). **(F)** Comparison of T_{Scd-S} for northern Caribbean (blue) and southern Caribbean (pink) with predictions of the preferred model (solid lines) and the corresponding 1D reference seismic models (*8*).

explore the predicted patterns in the strength of the computed seismic triplication. The observations of the D″ triplication in the Caribbean and central Pacific Ocean regions provide a good reference for testing the predictions. In the Caribbean, the *Scd* observations are very robust with an exception of the northeastern part, where there is no evidence for a triplication (*8*). In the central Pacific Ocean, the D″ triplication is weak and hardly detectable (*12*). The geographic patterns in the strength of the D″ triplication predicted by our preferred model (Fig. 5A) are in agreement with observations. The synthetic waveforms (Fig. 5B) are computed for three different paths. The strongest *Scd* amplitude is predicted for path C1 sampling D″ beneath the northwestern Caribbean (Fig. 1) where observations show that the D″ triplication is robust (*8*). The *Scd* amplitude for path C2 is significantly smaller. Such a weak triplication may be hard to detect in the observed waveforms, particularly when noise is present. The weakest *Scd* phase is predicted by our model for the path sampling the structure beneath the central Pacific Ocean. All these predictions are consistent with observations.

The predicted variations in the strength of the D″ triplication were produced entirely by variations of the local velocity gradients, because the discontinuity is present globally with the same amplitude. For example, there is a pronounced difference in the vertical seismic velocity gradients above the discontinuity (Fig. 2C). The gradient in the northwestern Caribbean (Fig. 2, left) is quite sharp, resulting in a strong seismic triplication. Beneath the northeastern Caribbean (Fig. 2, middle), the gradient above the discontinuity is smaller and the lateral extent of the high-gradient region intermittent; the combination of these factors leads to a much smaller *Scd* amplitude. Finally, the gradient above the discontinuity in the central Pacific Ocean (Fig. 2, right) is reduced by the slow velocity anomaly at the base of the mantle, and the strength of the predicted D″ triplication is substantially dampened.

The agreement of these trends with observations indicates that the D″ discontinuity may be a ubiquitous feature with the strength of the resulting seismic triplication modulated by larger scale structure. The variations of this structure produce strong variations in the predicted *Scd* amplitudes and can explain the apparent intermittance of the D″ discontinuity (*23*). However, local volumetric structure alone is insufficient to produce the observed regional variations of differential travel times (Fig. 4C) (*24*), requiring an added effect of the topography of the discontinuity. An important result of our modeling is that the topography of the D″ discontinuity must be correlated with the local volumetric velocity anomaly in a way that the discontinuity must be elevated in the faster-than-average regions and depressed in slower-than-average regions. This is implied by the positive values of Clapeyron slope providing a much better fit to the data (Fig. 3) than the negative values. This result provides a strong argument against the D″ discontinuity being on top of a chemically distinct layer at the base of the mantle (*25*) and further supports the phase transition mechanism for the discontinuity (*11, 26, 27*). Our model provides a prediction of the elevation of the D″ discontinuity above the CMB anywhere in the world (Fig. 1B). The disagreement between the predictions and the elevations inferred from 1D seismic studies illustrates the trade-offs between the location of the discontinuity and its larger scale structural context, and signifies the importance of considering structure in three dimensions with a proper account for the waveform perturbations caused by velocity variations along the whole ray path. At this stage, we have only examined the 2D predictions from our model. As tomographic images are sharpened, we would expect to see 3D effects along certain paths (*23*).

An important remaining issue about the possible phase transition at the base of the mantle is the mineralogical one. No relevant phase transition has yet been observed in the major elements of the lower mantle: (Mg,Fe)-SiO_3 (silicate perovskite) and (Mg,Fe)O (magnesiowüstite). However, several possibilities have been suggested (*28*). In addition, the moderate requirements for the effective change of properties of the mineral assemblage [as little as 1% associated increase in shear velocity and a minor volume change (*11, 27*)] allow for a phase transition in some of the minor mineralogical constituents of the D″ region. At the current rate of progress in experimental mineral physics, we should eventually be able to discover or rule out a phase transition at the top of D″, and these results should provide important guidance to such experiments.

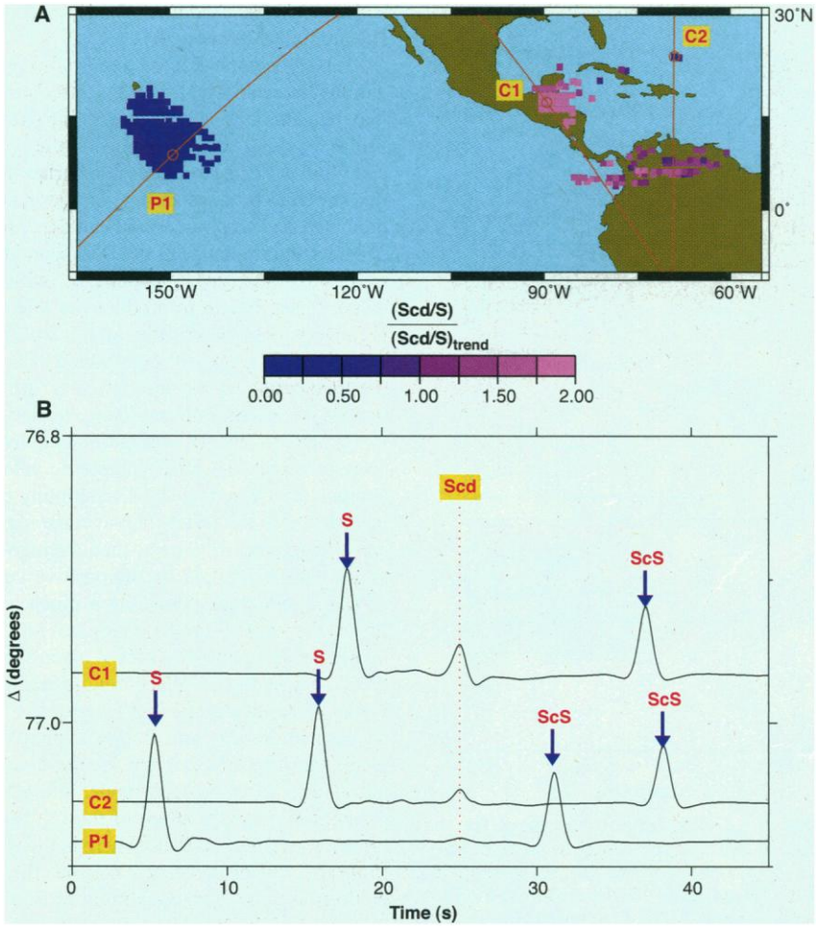

Fig. 5. Relative strength of the D″ triplication for the central Pacific Ocean and Central America predicted by the preferred model. (**A**) Geographical patterns. Each colored square has lateral dimensions of 1° by 1° and represents the average value of *Scd*:*S* amplitude ratios for all paths (Fig. 1) that have surface-projected *ScS* bounce points within the square. These values were normalized by the average distance trend (*35*). Paths C1, C2, and P1 (Fig. 1) are also shown. (**B**) Synthetic waveforms (Green's functions) computed for paths C1, C2, and P1 (cross sections along these paths are shown in Fig. 2). The waveforms are normalized by the amplitude of direct *S* and aligned by the *Scd* peak.

References and Notes

1. The most comprehensive global seismic velocity inversions are provided by seismic tomography (*13*). The characteristic features of all recent tomography models of the lower mantle are faster-than-average linear zones along the circum-Pacific belt and slow regions beneath the central Pacific Ocean and Africa. In many regions, the zones of fast velocity anomalies can be traced from the surface to the CMB and are probably associated with subducted slabs. The broad slow anomalies extend from the base of the mantle to at least 1500 km depth and may be indicative of hot upwellings.
2. T. Lay and D. V. Helmberger, *Geophys. J. R. Astron. Soc.* **75**, 799 (1983).
3. Q. Williams and E. J. Garnero, *Science* **273**, 1528 (1996).
4. M. E. Wysession *et al.*, *Science* **284**, 120 (1999).
5. Long-period *S*-wave studies allow for a 3% velocity increase over as much as 100 km. However, broadband studies limit the thickness of the transition zone to about 30 km [T. Lay and C. J. Young, *Geophys. Res. Lett.* **16**, 605 (1989)].
6. The D″ seismic discontinuity, first suggested in (*2*), explains an observed seismic triplication. The triplication is most pronounced in *S* waves, although it can sometimes be detected for *P* waves (*11*).
7. C. J. Young and T. Lay, *Phys. Earth Planet. Inter.* **49**, 37 (1987).
8. J.-M. Kendall and C. Nangini, *Geophys. Res. Lett.* **23**, 399 (1996).
9. J. B. Gaherty and T. Lay, *J. Geophys. Res.* **97**, 417 (1992); C. J. Young and T. Lay, *J. Geophys. Res.* **95**, 17385 (1990).
10. M. E. Wysession *et al.*, in *The Core-Mantle Boundary Region*, M. Gurnis, M. E. Wysession, E. Knittle, B. Buffett, Eds., *Geodynamics Series*, vol. 28 (American Geophysical Union, Washington, DC, 1998), pp. 273–297.
11. I. Sidorin, M. Gurnis, D. V. Helmberger, X. Ding, *Earth Planet. Sci. Lett.* **163**, 31 (1998).
12. A D″ triplication has been detected beneath the central Pacific Ocean, a region which is anomalously slow at the base of the mantle [S. Russell and T. Lay, *Eos (Fall Suppl.)* **79** (no. 45), 618 (1998)]. However, the triplication is extremely weak and only detectable by data stacking.
13. S. P. Grand, *J. Geophys. Res.* **99**, 11591 (1994); S. P. Grand, R. D. van der Hilst, S. Widiyantoro, *GSA Today* **7**, (no. 4) 1 (1997). Grand's shear velocity tomography model is parameterized by blocks with lateral dimensions of 2° by 2°. The blocks vary between 75 and 240 km in thickness, with the poorest resolution at the bottom of the mantle. For each block, a velocity perturbation with respect to PREM (Preliminary Reference Earth Model) (*29*) is provided.
14. I. Sidorin and M. Gurnis, in (*10*), pp. 209–230.
15. Although the observed local decorrelation between *P* and *S* velocity models may suggest some degree of chemical heterogeneity at the base of the mantle [for example, (*4*, *30*)], *S* and *P* velocities vary in phase in most regions [G. Masters, *11th Annual IRIS Workshop*, 9 to 12 June, Fishcamp, CA (Incorporated Research Institutions for Seismology, Washington, DC, 1999)]. This may imply a thermal origin of the velocity perturbations so that the local thermal anomaly can be inferred from the observed seismic velocity anomaly. A local velocity anomaly, ΔV, is mapped onto the thermal anomaly, ΔT, using $\Delta T = -2\Delta V/\alpha(h)/V_{PREM}(h)/(\Gamma - 1)$, where $\alpha(h)$ is the depth-dependent coefficient of thermal expansion computed following (*14*), $V_{PREM}(h)$ shear wave velocity corresponding to PREM (*29*), and $\Gamma \equiv (\partial G/\partial \rho)_p$ characterizes the temperature dependence of the shear modulus, *G*. We used $\Gamma = 6$ [D. L. Anderson, *Phys. Earth Planet. Inter.* **45**, 307 (1987)].
16. A phase transition is characterized by an ambient [corresponding to adiabatic temperature, or, in seismic velocity space, to PREM (*29*) values] elevation, h_{ph}, above the CMB and a Clapeyron slope, γ_{ph}, which controls the topography of the phase boundary when the local temperatures deviate from adiabatic. The phase at any given location can then be computed using [U. R. Christensen and D. A. Yuen, *J. Geophys. Res.* **89**, 4389 (1984)] $Z = 1/2[1 + \tanh(r_{ph}/w_{ph})]$, where w_{ph} (5 km) is the width of the phase transition and r_{ph} is given by $r_{ph}(h) = h - h_{ph} - \gamma_{ph}\,\Delta T/\rho(h)/g$. In the last equation, h is depth, g is the acceleration of gravity, and $\rho(h)$ is the density (*29*). The value of Z varies between 0 (low-pressure phase) and 1 (high-pressure phase).
17. The tomography model (*13*) is smoothed by interpolating the anomalies between the centers of the blocks. The smoothed structure is mapped onto a mesh with a 0.2° by 0.2° by 2 km resolution. A 1.5% velocity jump (*31*) is added to each vertical column of this fine mesh at a depth predicted by the phase transition characteristics (*16*). The addition of the discontinuity affects the predicted travel times, and to make our composite model consistent with the original tomography model, we applied a negative velocity gradient at the base of the mantle. In dynamic models, such a gradient is produced by a thermal boundary layer above the CMB (*14*). We used a constant velocity of 7 km/s (Fig. 2B) at the CMB and computed the gradient to preserve the travel time across the vertical column (*32*).
18. S. Ni, X. Ding, D. V. Helmberger, *Geophys. J. Int.*, in press.
19. The tomography model (*13*) has the poorest resolution at the very base of the mantle, so $T_{ScS\text{-}Scd}$ is less certain than $T_{Scd\text{-}S}$, because it includes the travel time of the *ScS* phase that traverses the D″ layer. In addition, our modification of the tomography model is restricted to the region below the imposed discontinuity (Fig. 2). This produces the largest disturbance on *ScS* travel times (*32*), further increasing the uncertainty in $T_{ScS\text{-}Scd}$.
20. The quality of agreement between the model predictions and observations can be characterized by the rms difference between predicted and observed $T_{Scd\text{-}S}$ differential travel times

$$\langle \delta T_{Scd\text{-}S} \rangle = \left[\frac{1}{N} \sum_{1}^{N} (T^{\,synth}_{Scd\text{-}S} - T^{\,data}_{Scd\text{-}S})^2 \right]^{1/2} \quad (1)$$

where N is the number of considered ray paths.
21. For Eurasia, Alaska, and India, we used the ray paths studied in (*7*, *9*). To explore the spatial variation of the triplication beneath the central Pacific Ocean and Central America, ray paths from three Fiji-Tonga and three South America events (*33*, *8*) to the World Wide Standard Seismograph Network (WWSSN) and the Canadian National Seismograph Network (CNSN) stations in North America in the 68° to 85° distance range were considered.
22. The D″ triplication has also been extensively studied beneath Central America. However, the structure beneath this region appears to be highly variable [for example, (*8*, *11*)], and no single comprehensive data set is currently available.
23. X. F. Liu, J. Tromp, and A. Dziewonski [*Earth Planet. Sci. Lett.* **160**, 343 (1998)] have suggested that the D″

discontinuity may be produced by the local gradients caused by thermal variations alone without a need for a first-order discontinuity. Although such a possibility has long been acknowledged by the seismological community (*10*), it is unlikely that thermal gradients of sufficient sharpness (*5*) can be produced. Dynamically consistent seismic velocity gradients constrained by mineral physics data (*11*) are not capable of producing a triplication consistent with observations. Similarly, no triplication is produced by the seismic velocity gradients obtained from tomography inversions (*18*).

24. This is not immediately obvious, considering some degree of smoothing that occurs in tomographic inversions [for example, L. Bréger, B. Romanowicz, L. Vinnik, *Geophys. Res. Lett.* **25**, 5 (1998)]. To test if a flat discontinuity combined with larger amplitude anomalies can produce travel time variations consistent with observations, we globally scaled the anomalies by a factor of 1.5. However, this did not significantly improve the fit to the observations.
25. Dynamic modeling incorporating a chemically distinct dense layer at the base of the mantle [for example, (*11*, *14*)] demonstrates that this layer is depressed beneath cold downwellings (likely corresponding to fast seismic velocity regions) and elevated beneath hot upwellings (slow velocity regions).
26. H.-C. Nataf and S. Houard, *Geophys. Res. Lett.* **20**, 2371 (1993).
27. I. Sidorin, M. Gurnis, D. V. Helmberger, *J. Geophys. Res.* **104**, 15005 (1999).
28. For example, L. Stixrude and M. S. T. Bukowinski [*J. Geophys. Res.* **95**, 19311 (1990)] have suggested that $(Mg,Fe)SiO_3$ may break down into oxides under D″ conditions; A. M. Hofmeister (in preparation) argued that the velocity jump at the top of D″ may be due to a MgO transition to NaCl or CsCl structure.
29. A. M. Dziewonski and D. L. Anderson, *Phys. Earth Planet. Inter.* **25**, 297 (1981).
30. R. D. van der Hilst and H. Kárason, *Science* **283**, 1885 (1999).
31. It has been demonstrated (*11*) that a jump of as little as 1% in velocity may explain the observations of the shear wave D″ triplication, provided it is accompanied by sufficiently large gradients. Here, we use a slightly higher value on the premise that tomographic inversion smears the structure so that the gradients provided by the tomography models are somewhat lower than in the real structure.
32. Adding the discontinuity and the low-velocity compensation at the base of the mantle only conserves travel times of phases that do not travel through D″ or cross D″ at steep angles. The imposed low-velocity zone would disturb the travel times of phases such as *ScS*, especially at large (>80°) distances when the phase almost grazes the CMB. At shorter distances however, only a small portion of the path is affected by the basal low-velocity zone and so the travel time perturbation is less significant.
33. E. J. Garnero, D. V. Helmberger, S. Grand, *Phys. Earth Planet. Inter.* **79**, 335 (1993).
34. The seismic 1D reference models for different regions were obtained in (7–9) to approximate the observed differential travel times for each particular region.
35. The normalization is required for a meaningful comparison of the relative strength of *Scd* phase for paths with different epicentral distances, since *Scd*/*S* increases with distance even for a constant seismic velocity structure (7–9). We obtain the distance trend by averaging *Scd*/*S* amplitude ratios for all ray paths with a given epicentral distance.
36. We thank S. Grand for access to his tomography model and T. Lay and E. Garnero for providing the D″ triplication travel time data. Two anonymous reviewers provided a number of valuable comments and suggestions. Supported by NSF grant EAR-9809771. This is contribution no. 8664, Division of Geological and Planetary Sciences, California Institute of Technology.

19 July 1999; accepted 14 October 1999

Fluid Flow in Chondritic Parent Bodies: Deciphering the Compositions of Planetesimals

Edward D. Young,[1]* Richard D. Ash,[1,2] Philip England,[1] Douglas Rumble III[2]

Alteration of the Allende meteorite caused shifts in oxygen isotope ratios along a single mass fractionation line. If alteration was caused by aqueous fluid, the pattern of oxygen isotope fractionation can be explained only by flow of reactive water down a temperature gradient. Down-temperature flow of aqueous fluid within planetesimals is sufficient to explain the mineralogical and oxygen isotopic diversity among CV, CM, and CI carbonaceous chondrites and displacement of the terrestrial planets from the primordial slope 1.00 line on the oxygen three-isotope plot.

Carbonaceous chondrites comprise seven distinct groups of primitive meteorites. The groups are distinguished on the basis of mineralogy, bulk elemental concentrations, and size and proportions of constituents such as chondrules and calcium-aluminum–rich inclusions (CAIs) (*1*). Each group is characterized by distinctive oxygen isotope ratios (*2*). The diversity in mineralogy and oxygen isotopic compositions is spanned by the CV, CM, and CI groups (*3*) and has been attributed to interactions among different primordial oxygen reservoirs on distinctive parent bodies with different geological histories (*4*). Here we show that reaction between rock and flowing water inside a carbonaceous chondrite parent body could have produced zones that resemble CV, CM, and CI meteorites in mineralogy and oxygen isotope ratios.

Studies of the Allende CV3 carbonaceous chondrite using the ultraviolet laser microprobe show that increases in $^{17}O/^{16}O$ and $^{18}O/^{16}O$ at constant $\Delta^{17}O$ on an oxygen three-isotope plot (*5*) (Fig. 1) are associated with alteration. The alteration is identified by localized enrichments in Fe, Cl, and Na and by growth of secondary minerals (*6*). Alteration occurred within several million years of chondrule and CAI formation about 4.5 billion years ago (*7*) and has been attributed either to reactions between vapor and solids in the early solar nebula (*8*) or to reactions between rock and liquid water at low temperatures within parent bodies that may have resembled some present-day asteroids (*9*).

The preponderance of evidence is that water had higher $\Delta^{17}O$ values than did coexisting anhydrous silicates in the early solar system (*10*). Laser ablation analyses showing that altered and unaltered components fall on a single mass fractionation curve (Fig. 1) suggest that the $\Delta^{17}O$ of the aqueous fluid (or any other reactant) responsible for the alteration was changed from its original value to the rock value by exchange of oxygen with the rock.

The exchange of oxygen between rock and a motionless aqueous fluid cannot explain the data in Fig. 1 because, when the amount of fluid is sufficiently small that its $\Delta^{17}O$ is controlled entirely by the rock, it has too little oxygen to change rock $\delta^{17}O$ and $\delta^{18}O$. This conundrum is quantified by means of the commonly used expression for the mass balance of oxygen between reacting rock (r) and stagnant water (w)

$$\frac{N_w}{N_r} = \frac{(\delta_r - \delta_r^0)}{\delta_w^0 - (\delta_r - \Delta)} \quad (1)$$

In Eq. 1, N is the number of oxygens composing the reacting water or rock; δ is the $\delta^{18}O$ or $\delta^{17}O$ for the indicated phase after reaction; δ^0 is $\delta^{18}O$ or $\delta^{17}O$ for the indicated phase before reaction; and Δ is the difference, $\delta_r - \delta_w$, between rock and water at equilibrium. The left side of Eq. 1 is referred to as the water-rock ratio. Because Eq. 1 applies to both $\delta^{17}O$ and $\delta^{18}O$, invariant rock $\Delta^{17}O$ during the exchange of oxygen between rock and water with different initial $\Delta^{17}O$ values is only possible in the limit, where the amount of oxygen composing the water relative to the amount of oxygen composing the rock is effectively zero

$$\lim_{(N_w/N_r) \to 0} (\delta_r - \delta_r^0) = 0 \quad (2)$$

Equations 1 and 2 show that reaction between static water and rock could not have shifted rock $\delta^{18}O$ at fixed $\Delta^{17}O$ as indicated by the data in Fig. 1 unless the water and rock had

[1]Department of Earth Sciences, University of Oxford, Parks Road, Oxford, OX1 3PR, UK. [2]Geophysical Laboratory, Carnegie Institution of Washington, 5251 Broad Branch Road NW, Washington DC, 20015, USA.

*To whom correspondence should be addressed. E-mail: ed.young@earth.ox.ac.uk

References and Notes

[3] **Seismic Evidence for Partial Melt at the Base of Earth's Mantle**
Quentin Williams; Edward J. Garnero
Science, New Series, Vol. 273, No. 5281. (Sep. 13, 1996), pp. 1528-1530.
Stable URL:
http://links.jstor.org/sici?sici=0036-8075%2819960913%293%3A273%3A5281%3C1528%3ASEFPMA%3E2.0.CO%3B2-C

[4] **Lateral Variations in Compressional/Shear Velocities at the Base of the Mantle**
Michael E. Wysession; Amy Langenhorst; Matthew J. Fouch; Karen M. Fischer; Ghassan I. Al-Eqabi; Patrick J. Shore; Timothy J. Clarke
Science, New Series, Vol. 284, No. 5411. (Apr. 2, 1999), pp. 120-125.
Stable URL:
http://links.jstor.org/sici?sici=0036-8075%2819990402%293%3A284%3A5411%3C120%3ALVICVA%3E2.0.CO%3B2-P

[30] **Compositional Heterogeneity in the Bottom 1000 Kilometers of Earth's Mantle: Toward a Hybrid Convection Model**
Rob D. van der Hilst; Hrafnkell Kárason
Science, New Series, Vol. 283, No. 5409. (Mar. 19, 1999), pp. 1885-1888.
Stable URL:
http://links.jstor.org/sici?sici=0036-8075%2819990319%293%3A283%3A5409%3C1885%3ACHITB1%3E2.0.CO%3B2-X